Aerospace Science and Technology 139 (2023) 108356

Contents lists available at ScienceDirect

Aerospace Science and Technology

journal homepage: www.elsevier.com/locate/aescte

The response mechanism of pressure fluctuation to the unsteady heat release in a strong rotating environment

Shoujun Ren [a,b,*], Bo Tian [c], William P. Jones [a], Xiaohan Wang [b]

[a] Department of Mechanical Engineering, Imperial College London, Exhibition Road, London, SW7 2AZ, UK
[b] Guangzhou Institute of Energy Conversion, Chinese Academy of Sciences, Guangzhou, 510640, China
[c] Department of Engineering, University of Leicester, University Road, Leicester, LE1 7RH, UK

ARTICLE INFO

Article history:
Received 11 July 2022
Received in revised form 2 March 2023
Accepted 19 April 2023
Available online 2 May 2023
Communicated by Suresh Menon

Keywords:
Response mechanism
Vortex-tube combustor
Momentum flux
Uneven attenuation
Centrifugal weight coefficient

ABSTRACT

The response mechanism of the pressure fluctuation to the unsteady heat release rate at the 'unsteady' combustion state in a strong rotating environment was investigated using a stratified vortex-tube combustor via a large eddy simulation method. Results show that the peak amplitude of heat release fluctuation at the 'unsteady' state is just 2.8×10^6 W/m^3 and the peak amplitude of pressure fluctuation is always within 3000 Pa based on the vortex-tube configuration, indicating a weak fluctuation degree. The unsteady heat release does not bring about a higher momentum flux fluctuation due to quick momentum damping in the rotating reactive environment. The pressure fluctuation does not relate closely to the momentum flux and its fluctuation; this is due to the effect of the centrifugal force caused by rotating behavior. After splitting the momentum flux into the different components, we found that the tangential component acts in reverse to that of the radial and axial directions in the exterior region. Viz., the pressure increases when the tangential momentum flux increases in the exterior region but decreases when the radial and axial components increase. The laminarization of the fluid suppresses the fluctuations in the radial and axial directions only, therefore the uneven attenuation of the momentum flux fluctuation in different directions is the dominant cause of the enlarged pressure fluctuation in the 'unsteady' burning state. Moreover, we find that the pressure fluctuation degree is also closely related to the centrifugal weight coefficient. When this coefficient is far away from zero, the centrifugal effect will become obvious, and vice versa.

1. Introduction

Combustion stabilization is crucial to improving the performance of gas turbines, engines, and various industrial combustors under extreme conditions [1]. Good stabilization can increase the operating limit and the service life of the equipment. Research on the driving mechanism of pressure fluctuation has important guiding significance and reference value for the control of instability combustion or pressure fluctuation, yielding a steady combustion process. The flame dynamic or the unsteady heat release is known to be responsible for thermo-acoustic coupling and combustion instability. So, understanding the functional mechanism of unsteady heat release is of great significance to controlling the effect of flame dynamics and achieving an ultra-steady combustion process. For this study when the amplitude of the pressure fluctuation is within 2% of the operating pressure, viz., 2000 Pa, the corresponding combustion is regarded as an ultra-steady combustion process.

The combustion driving mechanisms of pressure fluctuation have been investigated in our past work [2] using a stratified vortex-tube combustor, wherein the effects of flame-, aero-, and thermo-dynamics have been analyzed and discussed. We found that when the unstable inertial force in a field is stronger than the viscous and centrifugal forces combined with the density gradient, the amplitude of pressure fluctuation will increase and instability is likely to arise. It has been shown that the unstable inertial force depends on the Reynolds number (or Taylor number) and the unsteadiness of the heat release. The inertial force, which can be suppressed by increasing the rotation motion and density gradient, has already received wide coverage in the existing literature [3,4].

The effect of unsteady heat release is usually quantified by the Rayleigh parameter [5,6] and the flame transfer or describing function [7–9]. Lieuwen et al., have pointed out that when the Rayleigh number $Ra(x)$ is larger than 0, the thermo-acoustic coupling will occur, yielding self-exciting combustion [6]. In our

* Corresponding author.
E-mail address: sren.combust@gmail.com (S. Ren).

https://doi.org/10.1016/j.ast.2023.108356

Nomenclature

a	Absolute acceleration
A_T	Total sectional area of tangential inlet slits
D_e	Exit throat diameter
D_o	Diameter of the combustion tube
EXP	Experimental results
F	Net force
FTF	Flame transfer function
G_A	Exit axial momentum
G_ω	Input angular momentum
h	Enthalpy
HRR	Heat release rate
LES	Large-eddy simulation
m	Mass
N	Number of stochastic fields
Ns	Number of species
p	Pressure
p_0	Local pressure ignored centrifugal effect
pdf	Probability density function
p_k	Peak pressure
Pr	Prandtl number
q_f	Fuel flow rate .... L/min
r	Radial position from the tube center
ra	Radial and axial coupling
R	Momentum radius vector
$Ra(x)$	Rayleigh number
R_i^*	Stratification parameter
S	Swirl number
Sc	Schmidt number
sgs	Sub-grid-scale
t	Time
T	Temperature
u	Flow velocity
u_a	Axial velocity
u_c	Radial and axial coupling velocity
u_t	Tangential velocity
ρu^2	Momentum flux
ρu_t^2	Tangential momentum flux
ρu_c^2	Radial and axial coupling momentum flux
x, y, z	Coordinate axis
Y_α	Mole number of chemical species

Greek

α	Species
φ	Equivalence ratio
φ_g	Global equivalence ratio
ϕ_α	Mole number of the α-th chemical species or the enthalpy
ρ	Density
$\triangle$	Value difference
λ	Centrifugal weight coefficient
δ_{ij}	Kronecker delta
σ	Prandtl/Schmidt number
τ	Integration time
τ_{ij}	Stress tensor
μ	Dynamic viscosity

past research, the $Ra(x)$ number has been calculated to quantify the impact of unsteady heat release upon the unsteadiness of the combustion [10]; this paper showed that when the $Ra(x)$ number is larger than 0.1, the amplitude of pressure fluctuation exceeds 2000 Pa, yielding relatively unsteady combustion. Additionally, the flame transfer function (*FTF*) studied by Candel et al. can quantitatively reflect the contribution that unsteady heat release also has on pressure fluctuation [11]. However, neither of these two methods can reveal what the most essential reason for pressure fluctuation is, nor the response mechanism of the pressure fluctuation to unsteady heat release. Instead, the effect of unsteady heat release is simply quantified by the Rayleigh number and flame transfer function without an in-depth analysis of the causes of pressure fluctuation from the mechanism point of view.

Given that heat release will affect temperature distribution, thermal expansion will decrease the density and increase the local velocity based on the conservation of momentum theory. Further, turbulent kinetic energy is positively correlated with velocity squared, therefore the thermal expansion will increase the turbulent kinetic energy, in theory bringing about a greater degree of fluctuation. The same conclusion can also be obtained through an analogy with the ideal gas state equation [12]. As is well known, a swirling environment is helpful in improving combustion stability, which is widely used in various industrial combustors, engines, and gas turbines. There are indications that the vortex-tube combustion technique has good aero-dynamic [13] and thermo-dynamic [14] stability due to its strong rotating behavior and large density gradient. The generated large body force can suppress the pressure fluctuation and lead to the laminarization of the flow field. However, the thermo-acoustic response mechanism will be more complicated due to the effect of centrifugal force in the strong swirling environment. Moreover, the strong rotating behavior will also lead to a strong momentum exchange [4], which can also promote the transport and reduction of turbulent kinetic energy or momentum.

Therefore, the resultant good aero- and thermo- dynamic stabilities and large momentum damping rate are a good indication of the potential to suppress kinetic energy disturbance caused by unsteady heat release or flame-dynamic. These are also the principal reasons for the good stabilization of the vortex-tube combustion technique. However, for some extreme conditions, the peak amplitude of pressure fluctuation is still over 2000 Pa, which, for some highly demanding industrial combustors or engines [15], requires further suppression.

This investigation of the transfer mechanism from unsteady heat release to pressure fluctuation in a strong swirling environment is helpful for controlling the influence of unsteady heat release on the high amplitude of pressure fluctuation or instability from the very beginning. It provides theoretical guidance and reference value for the suppression of high-pressure fluctuations that result from the influence of flame dynamics. The pressure, density, and momentum flux at different points were investigated to analyze the response mechanism of the pressure fluctuation to the unsteady *HRR* in a strong rotating environment via the LES simulation method. In the result section, the relationship between the fluctuations of pressure, heat release rate, and momentum flux will be exhibited. And then in the discussion section, the transfer mechanism from unsteady heat release to pressure fluctuation in a strong swirling environment will be analyzed and summarized. The corresponding discoveries may provide significant information to reduce pressure fluctuation and achieve an ultra-steady combustion process.

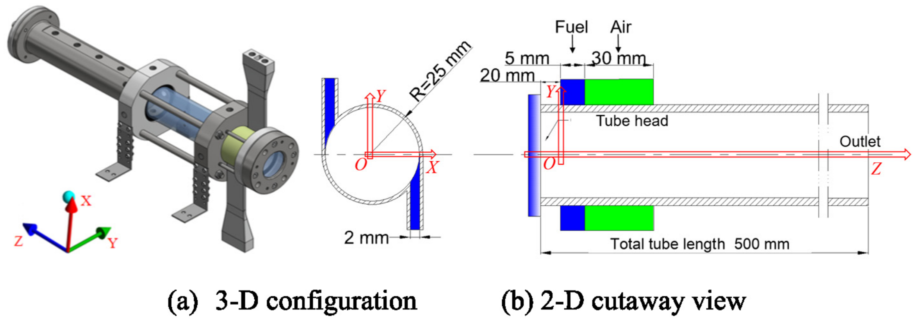

Fig. 1. Configuration of the vortex-tube combustor.

Table 1

Points and location	7	8	9	10	11	12	60	61
x [mm]	0	0	0	0	0	0	0	0
y [mm]	23.55	20.49	18.05	17.65	16.70	11.20	24.00	14.00
z [mm]	14.40	16.00	20.00	21.50	23.20	30.00	60.00	60.00

2. Physical model of the combustor and research method

2.1. Physical model and boundary conditions

The structure of the vortex-tube combustor is displayed in Fig. 1. It consists of one combustion tube and four tangential slits. The fuel and oxidant inject into the combustion tube tangentially and separately, and then the fuel and oxidant mix with each other. The diameter, tube length, and slit width of this combustor are 50.0, 500.0, and 2.0 mm, respectively, and the fuel and air slit lengths are 5.0 and 30.0 mm, respectively. The air slit is immediately downstream of the fuel slit. The swirl number of this combustor is 13.46 based on Eq. (1). $z = 0$ mm is located in the position of the beginning of the fuel slit along the axial direction.

$$S \equiv \frac{G_\omega}{RG_A} \approx \frac{\text{Input Angular Momentum}}{\mathrm{D}_e/2 \times \text{Exit Axial Momentum}} = \frac{\pi D_e D_o}{4A_T} \tag{1}$$

where D_o is the diameter of the combustion tube, D_e is the exit throat diameter, and A_T is the total sectional area of the tangential inlet slits.

Given that ethanol is a renewable source of energy that can be obtained from a wide range of sources, it is beneficial to change the energy structure by adopting ethanol, in pursuit of achieving carbon neutrality. Gaseous ethanol of 400 K is employed as the fuel and air of 300 K is employed as the oxygen. The fuel and oxygen are both injected into the combustor via their respective slits. The global equivalence ratio is defined as φ_g, which accounts for all the fuel and oxygen injected into the combustor. The fuel flow rate is denoted as q_f. Based on the amplitudes of the pressure fluctuations in different cases, the case of $q_f = 54.0$ L/min and $\varphi_g = 0.48$ was selected for the 'unsteady' combustion condition, and the case of $q_f = 9.0$ L/min and $\varphi_g = 0.5$ was selected for the steady combustion condition under ordinary pressure ($p = 1.01 \times 10^5$ Pa). The definition and selection of steady and 'unsteady' combustion will be elaborated on in detail in the Result section. The fluctuation information is recorded at points 7-12 and 60-61, in terms of the velocity (u), density (ρ), temperature (T), and pressure (p). The location of the different points is detailed in Table 1.

2.2. Mathematical modeling

In the simulation, the computational domain is determined according to the actual combustor size exactly, which consists of four tangential slits and a constant-diameter tube, as seen in Fig. 2.

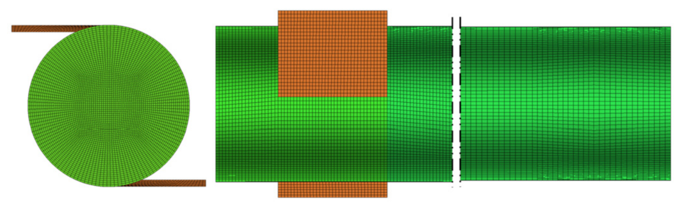

Fig. 2. The computational domain of the SVC.

A structured three-dimensional (3-D) hexahedral grid with 2.5 million elements is employed as the computational domain after the independent mesh verification, wherein the meshes with 0.5, 1.0, 1.5, 2.0, 2.5, and 3.0 million nodes were employed. The distributions of temperature, species, and heat release rate were compared under different mesh quantities. It turns out that the difference between the solutions with 2.5 and 3.0 million mesh cells is within 0.5%. Thus, 2.5 million cells are adopted in the paper.

The grid quality is above 0.85 and the y^+ near the tube wall is 1.0. The computational domain is determined according to the actual combustor size. The chemical kinetics mechanism employed for the oxidation of methane is the reduced mechanism proposed by Lu et al. [16] based on the GRI-Mech 3.0 mechanism, which consists of 19 chemical species and 15 reaction steps. This is used for the LES verification section. The chemical kinetic mechanism for the oxidation of ethanol consists of 28 chemical species and 180 reaction-steps [17], which is capable of predicting a wide range of complex flame phenomena.

The in-house block-structured, parallel, compressible LES code Boundary Fitted Flow Integrator (BOFFIN-LESc) has been used in this work. In LES, the equations of motion are solved directly for the resolved large-scale turbulent motions and eight stochastic fields are employed to account for sub-grid scale fluctuation in the species or enthalpy formation rates. Soret and Dufour's effects have been neglected in this work and all gases obey the ideal gas law. The fluid-structure coupling effect is ignored to simplify the analysis. Radiative heat transfer is considered through a radiation model described in [18]. The unburnt species inlet boundary condition is the volume flow rate condition. The burnt species outlet boundary condition is the pressure outlet condition. The computational time step varies from 1.0 to 15.0 $\times$ 10^{-7} s using a constrained Courant-Friedrichs-Lewy (***CFL***) number that is below 0.3 based on the flow velocity and the character mesh dimension.

In the field of continuum mechanics, the evolution of any given fluid flow can be described by a set of coupled non-linear partial differential equations (PDEs) based on the laws of mass, momentum, and energy conservation.

2.2.1. Large-eddy simulation-filtered conservation equations

Continuity:

$$\frac{\partial \overline{\rho}}{\partial t} + \frac{\partial \overline{\rho}\widetilde{u}_j}{\partial x_j} = 0 \tag{2}$$

where t is the time, $\widetilde{u}_j$ and x_j denote the velocity and spatial coordinate in the j direction, respectively, and $\overline{\rho}$ indicates the fluid density.

Momentum:

$$\begin{aligned} &\frac{\partial \overline{\rho}\widetilde{u}_i}{\partial t} + \frac{\partial \overline{\rho}\widetilde{u}_i\widetilde{u}_j}{\partial x_j} = -\frac{\partial \overline{p}}{\partial x_i} \\ &+ \frac{\partial}{\partial x_j}\left[-\frac{2}{3}\mu\frac{\partial \overline{u}_k}{x_k}\delta_{ij} + \mu\left(\frac{\partial \overline{u}_i}{\partial x_j} + \frac{\partial \overline{u}_j}{\partial x_i}\right)\right] - \frac{\partial \tau_{ij}^{sgs}}{\partial x_j} \end{aligned} \tag{3}$$

where p is the pressure, δ_{ij} denotes the Kronecker delta, the filtered product $\widetilde{u_i u_j}$ differs from the product of filtered velocities $\widetilde{u}_i\widetilde{u}_j$, τ_{ij}^{sgs} denotes the sub-grid scale (*sgs*) stress tensor, which is determined via the Smagorinsky model [19] and can be calculated using the following equation:

$$\tau_{ij}^{sgs} = \overline{\rho}\left(\widetilde{u_i u_j} - \widetilde{u}_i\widetilde{u}_j\right) \tag{4}$$

Mass (species):

$$\frac{\partial \overline{\rho}\widetilde{Y}_\alpha}{\partial t} + \frac{\partial \overline{\rho}\widetilde{u}_j\widetilde{Y}_\alpha}{\partial x_j} = -\frac{\partial}{\partial x_j}\left(\left(\frac{\mu}{Sc} + \frac{\mu_{sgs}}{Sc_{sgs}}\right)\frac{\partial \widetilde{Y}_\alpha}{\partial x_j}\right) + \overline{\rho\dot{\omega}_\alpha} \tag{5}$$

where μ is dynamic viscosity, Sc indicates the Schmidt number, $\widetilde{Y}_\alpha$ denotes the specific mole number of the α-th chemical species, the $\widetilde{Y}_\alpha = [Y_1, \ldots, Y_{Ns}]$, where Ns denotes the number of scalars ($1 \leq \alpha \leq Ns$), the subscript *sgs* indicates the sub-grid scale values, and $\overline{\rho\dot{\omega}_\alpha}$ represents the formation rates (sources) of species.

Enthalpy:

$$\frac{\partial \overline{\rho}\widetilde{h}}{\partial t} + \frac{\partial \overline{\rho}\widetilde{u}_j\widetilde{h}}{\partial x_j} = \frac{\partial \overline{p}}{\partial t} + \widetilde{u}_i\frac{\partial \overline{p}}{\partial x_i} - \frac{\partial}{\partial x_j}\left(\left(\frac{\mu}{Pr} + \frac{\mu_{sgs}}{Pr_{sgs}}\right)\frac{\partial \widetilde{h}}{\partial x_j}\right) \tag{6}$$

where $\widetilde{h}$ denotes the specific enthalpy, including enthalpies of formation, and Pr indicates the Prandtl number.

2.2.2. Joint sgs-pdf and stochastic fields approach

Due to the difficulties encountered in evaluating the filtered values of the chemical source terms, the equations (5) and (6) are not solved directly but rather an approach based on a modeled evolution equation for the spatially filtered joint fine-scale probability density function (*pdf*) is adopted [20], as modified by Brauner et al. [21]. The solution to this will yield all the spatially filtered one-point moments of the scalars involved. The joint *sgs pd* equation formulation f, denoted as $\widetilde{P}_{sgs}$, is introduced to represent the filtered product of the fine-grained *pdf* of each scalar, i.e., the specific mole numbers of the chemical species and the enthalpy.

$$\widetilde{P}_{sgs}(\psi; x, t) = \frac{1}{\overline{\rho}}\int_\Omega \rho G((x - x'), \Delta x)\Gamma(\psi; x', t)dx' \tag{7}$$

where Γ denotes the joint *sgs-pdf*, x is the spatial location, G is the filter function, Ψ indicates the scalar, and Ω indicates that the integration is defined over the entire flow domain.

The exact equation describing the evolution of the *pdf* can be derived by standard methods, for example, those employed by Gao and O'Brien [22] and Jaberi et al. [23]. Based on the approach of Brauner et al. [21], the resolved part of the convection and 'molecular' mixing are added to both sides of the equation, thus the modeled joint-*pdf* evolution equation becomes:

$$\begin{aligned} &\overline{\rho}\frac{\partial \widetilde{P}_{sgs}(\psi)}{\partial t} + \overline{\rho}\widetilde{u}_i\frac{\partial \widetilde{P}_{sgs}(\psi)}{\partial x_j} + \sum_{\alpha=1}^{Ns+1}\frac{\partial}{\partial \psi_\alpha}\left[\overline{\rho\dot{\omega}_\alpha(\psi)}\widetilde{P}_{sgs}(\psi)\right] \\ &+ \sum_{\alpha=1}^{Ns+1}\sum_{\beta=1}^{Ns+1}\frac{\mu}{\sigma}\frac{\partial \overline{\phi_\alpha}}{\partial x_j}\frac{\partial \overline{\phi_\beta}}{\partial x_j}\frac{\partial^2 \overline{P_{sgs}(\psi)}}{\partial \psi_\alpha \psi_\beta} \\ &= \frac{\partial}{\partial x_j}\left[\left(\frac{\mu}{\sigma} + \frac{\mu_{sgs}}{\sigma_{sgs}}\right)\frac{\partial \widetilde{P}_{sgs}(\psi)}{\partial x_j}\right] \\ &- \frac{C_d}{\tau_{sgs}}\sum_{\alpha=1}^{Ns+1}\frac{\partial}{\partial \psi_\alpha}\left[\overline{\rho}\left(\psi_\alpha - \widetilde{\phi}_\alpha(x,t)\right)\widetilde{P}_{sgs}(\psi)\right] \end{aligned} \tag{8}$$

where $\widetilde{\phi}_\alpha$ denotes either the specific mole number of the α-th chemical species or the enthalpy, ψ denotes the phase space of the scalar $\widetilde{\phi}_\alpha$, $J_{\alpha,j}$ is the species diffusion flux based on Fick's law, C_d represents the micro-mixing constant with a value of 2.0 [24], the σ_{sgs} value is 0.7 [25], and value of μ_{sgs} is produced by the Smagorinsky model and can be obtained via the following equation:

$$\mu_{sgs} = \overline{\rho}(Cs\Delta)^2\left\|\widetilde{S}_{ij}\right\| \tag{9}$$

where S_{ij} denotes the strain tensor, C_s represents the Smagorinsky parameter, which can be obtained through the dynamic process of Piomelli and Liu [26], and τ_{sgs} refers to the micro-mixing time scale, which is assumed to be given by [27]:

$$\tau_{sgs}^{-1} = C_d\frac{\mu + \mu_{sgs}}{\overline{\rho}\Delta^2} \tag{10}$$

where Δ denotes the filter width, which is taken as the cube root of the local grid cell volume.

Given that it is not feasible to numerically solve the closed form of the pdf evolution equation, Eq. (7) is solved using the Eulerian stochastic field method, where the $\widetilde{P}_{sgs}(\psi)$ is represented by an ensemble of N stochastic fields for each of the $Ns+1$ scalars, viz., $\xi_\alpha^n(x,t)$ with $1 \leq n \leq N$, $1 \leq \alpha \leq Ns+1$. The joint *sgs-pdf* equation (Eq. (7)) can therefore be expressed as follows:

$$\begin{aligned} &\widetilde{P}_{sgs}(\psi; x, t) \\ &= \frac{1}{N}\sum_{n=1}^{N}\frac{1}{\overline{\rho}}\int_\Omega \rho G((x - x'), \Delta x) \times \prod_{\alpha=1}^{Ns+1}\delta\left[\psi_\alpha - \xi_\alpha^n(x,t)\right]dx' \end{aligned} \tag{11}$$

In this work, the Itô formulation of the stochastic integral is employed, and thus the stochastic fields can evolve according to [28]:

$$\begin{aligned} &\overline{\rho}d\xi_\alpha^n + \overline{\rho}\widetilde{u}_j\frac{\partial \xi_\alpha^n}{\partial x_j}dt = \frac{\partial}{\partial x_j}\left[\left(\frac{\mu}{\sigma} + \frac{\mu_{sgs}}{\sigma_{sgs}}\right)\frac{\partial \xi_\alpha^n}{\partial x_j}\right]dt \\ &+ \sqrt{2\overline{\rho}\frac{\mu_{sgs}}{\sigma_{sgs}}}\frac{\partial \xi_\alpha^n}{\partial x_j}dW_j^n - \frac{C_d\overline{\rho}}{2\tau_{sgs}}\left(\xi_\alpha^n - \widetilde{\phi}_\alpha\right)dt + \overline{\rho}\dot{\omega}_\alpha^n\left(\xi^n\right)dt \end{aligned} \tag{12}$$

where the final term on the right-hand side is $(D\overline{p}/Dt \times dt)$ for the scalar of total enthalpy and the net formation rate through a chemical reaction in the case of chemical species; σ indicates the Prandtl/Schmidt number; and dW_j^n indicates the increments of a vector Wiener process, which is different for each field but independent of the spatial location, x, and is approximated by time-step increments $\eta_j^n\sqrt{dt}$ containing the {-1, 1} dichotomic random

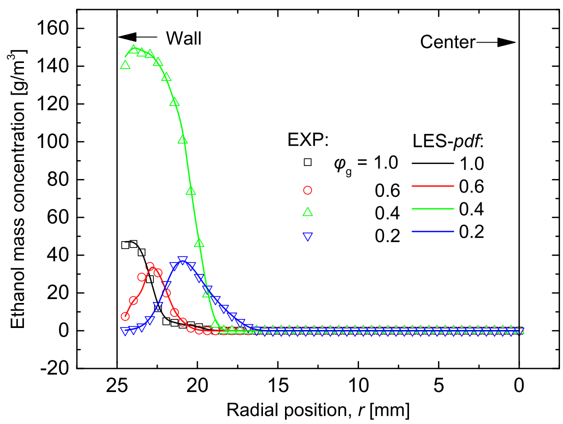

Fig. 3. The ethanol concentration verification at different φ_g and q_f = 12.0 L/min.

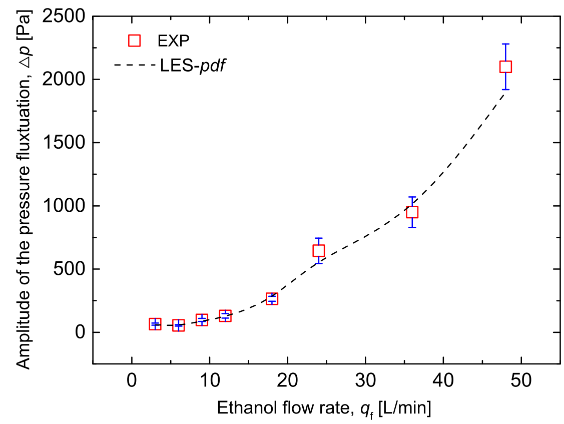

Fig. 4. The pressure fluctuation verification at different q_f and $\varphi_g = 0.5$.

vector η_j^n. The solutions of the stochastic fields equation are continuous, differentiable, and smooth on the scale of the filter width in space and continuous but not differentiable in time. The Favre filtered value of the reactive scalar, $\widetilde{\phi}_\alpha$ can be calculated by averaging over the stochastic fields:

$$\widetilde{\phi}_\alpha = \frac{1}{N}\sum_{n=1}^{N}\xi_\alpha^n \tag{13}$$

2.3. LES-*pdf* validation

In this section, the mathematical modeling described above is verified through a comparison of the corresponding results with the experimental results by taking methane as fuel under the same boundary condition. The flame topology and flame structure have been verified in previously published work by taking methane as fuel [29]. The binary flame structure can be reliably reproduced via this LES-*pdf* model and the flame diameter, length, and bifurcation of the LES-*pdf* method also show good dependability when compared with the experiment. The fuel employed in this work is ethanol; the ethanol species distributions under different φ_g at q_f = 12.0 L/min were verified further and the corresponding results are displayed in Fig. 3. The experiment was conducted in earlier works, wherein the corresponding experimental equipment is the same as that used in our previous published papers [14,30].

Fig. 4 exhibits the amplitudes of pressure fluctuation of the LES-*pdf* calculation and experiment results at point 1 in different thermal output cases under $\varphi_g = 0.5$ for the methanol combustion. It can also be observed that the amplitude of the pressure fluctuation of the LES-*pdf* result correlates satisfactorily with that of the experiment. The maximum deviation is always within 2%. This indicates that the LES-*pdf* method has strong reliability.

3. Results

Based on the pressure fluctuations in this combustor, we found that the amplitude of pressure fluctuation, $\triangle p$, ranges from 40 ∼ 3000 Pa, always within 5% of the operating pressure, thus, strictly speaking, the combustion in the entire combustion map is steady in this combustor [31]. However, given the large difference between the cases, the combustion process was divided into two categories: one is ultra-steady combustion ($\triangle p < 2000$ Pa) and the other is 'unsteady' combustion ($2000 < \triangle p < 5000$ Pa). Given the 'unsteady' combustion is not exactly unsteady combustion, quotation marks are used throughout.

Fig. 5 shows the pressure and heat release rate, *HRR*, fluctuations under steady-state conditions at q_f = 9.0 L/min and $\varphi_g = 0.5$ and the 'unsteady' state at q_f = 54.0 L/min and $\varphi_g = 0.48$. Fig. 5a shows that the amplitude of pressure fluctuation, $\triangle p$, at a steady state is around 70 Pa, whilst the amplitude of volume-averaged *HRR* fluctuation, △*HRR*, is just 5 × 10^5 W/m^3, indicating a highly steady combustion process. However, for the case of q_f = 54.0 L/min and $\varphi_g = 0.48$, the $\triangle p$ can reach nearly 3000 Pa, which is about 43.0 times greater than that of the steady state, whilst the △*HRR* also shows an obvious increase: it is 5.6 times greater than that of the 'unsteady' state, as seen in Fig. 5b, indicating an 'unsteady' combustion process. The Rayleigh parameter $Ra(x)$ at different combustion states is also calculated based on Eq. (14). The resultant $Ra(x)$ in the 'unsteady' state is 6.98 × 10^{-2}, which is positive and much larger than that at the steady state of 2.55 × 10^{-4}. Thus, thermo-acoustic coupling should arise in this case.

$$Ra(x) = \frac{1}{\tau}\int_{\tau} p'(t)q'(t)dt \tag{14}$$

where t and τ are time and integral time, respectively.

Fig. 6 exhibits the spectral analysis of the pressure and *HRR* fluctuations under steady and 'unsteady' states, which results from the Fourier transform of pressure and heat release fluctuations. Fig. 6a shows that there is nearly no obvious peak in the steady state for both pressure and heat release fluctuations. However, there are several peaks at different frequencies for both pressure and heat release in the 'Unsteady' state as seen in Fig. 6b, whilst the peak frequency of heat release fluctuation is very similar to that of pressure fluctuation, indicating a good thermo-acoustic coupling [6], which is also one of the main reasons that the $Ra(x)$ of the 'unsteady' state is much larger than that in the steady-state mentioned in the last paragraph. The frequency of the smallest one is 288 Hz, the second peak is located at 3900 Hz position, and correspondingly the frequency of the third to fifth peaks are around 8000, 12000, and 16000 Hz, respectively.

It is worth noting that even in the 'unsteady' combustion state, the pressure fluctuation amplitude $\triangle p$ is still within 5% of the operating pressure and the Rayleigh parameter is just 6.98 × 10^{-2}, indicating a weak degree of thermo-acoustic coupling and a good stabilization performance of this combustor.

Fig. 7 exhibits the pressure and momentum flux, ρu^2, at q_f = 54.0 L/min and $\varphi_g = 0.48$. Figs. 7a and 7b display the data under the cold state and burning state, respectively. Fig. 7a indicates that the $\triangle p$ is approximately 2000 Pa, which is smaller than that in the burning state. However, an interesting phenomenon was discovered. Based on the momentum flux theory, the amplitude of pressure fluctuation $\triangle p$ should be proportional to the momentum flux and the pressure should generally decrease with the increase

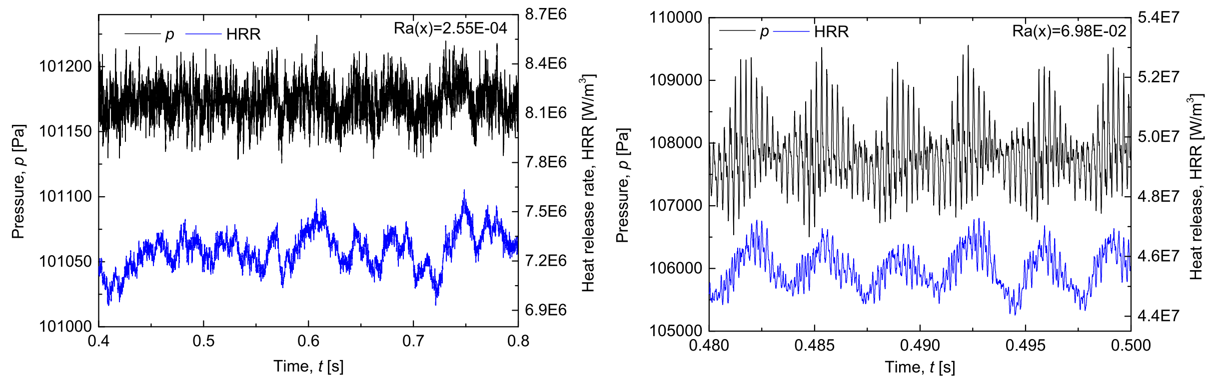

(a) Steady state: $q_f = 9.0$ L/min and $\varphi_g = 0.5$

(b) 'unsteady' state: $q_f = 54.0$ L/min and $\varphi_g = 0.48$

Fig. 5. The pressure and *HRR* fluctuations under steady and 'unsteady' states: (a) Steady state, (b) 'Unsteady' state. (For interpretation of the colors in the figure(s), the reader is referred to the web version of this article.)

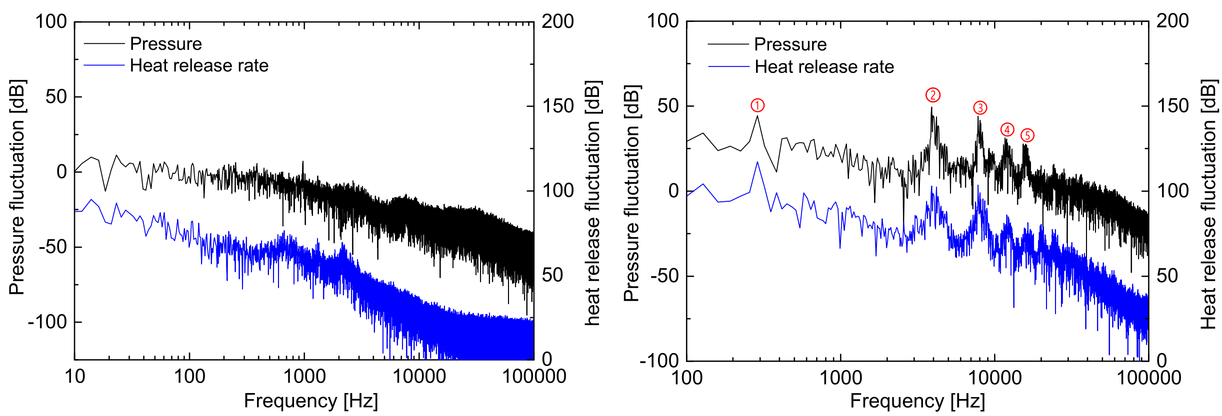

(a) Steady-state: $q_f = 9.0$ L/min and $\varphi_g = 0.5$

(b) 'Unsteady' state: $q_f = 54.0$ L/min and $\varphi_g = 0.48$

Fig. 6. The spectral analysis of the pressure and HRR fluctuations under steady and 'unsteady' states: (a) Steady state, (b) 'Unsteady' state.

of momentum flux ρu^2. The momentum flux indicates the pressure fluctuation of a fluid element, according to the derivation below:

$$\begin{aligned} & Ft = -mu \Rightarrow \Delta Ft = -\Delta mu \Rightarrow \Delta pAt = -\Delta mu \\ & \Rightarrow \Delta p = -\frac{\Delta mu}{At} \\ & \Rightarrow \Delta p = -\Delta \rho u^2 \end{aligned} \quad (15)$$

where m is mass, F is net force, u is the fluid velocity, t is time.

However, from Fig. 7 it can be obtained that the amplitude of momentum flux ρu^2 fluctuation at the cold state is larger than that of the burning state. The $\triangle \rho u^2$ under the cold state is already beyond 2×10^4 kg/(m · s^2), while the $\triangle \rho u^2$ under the burning state is just 1.5×10^4 kg/(m · s^2). This is contrary to the generally accepted understanding. Moreover, Fig. 7 also indicates that the pressure does not decrease when the momentum flux ρu^2 increases; the opposite effect can be observed in Fig. 7b. Therefore, with these questions and contradictions in mind, an in-depth discussion was carried out.

4. Discussion

4.1. Momentum flux and weak correlation

Given that the flow direction is from the tube wall to the center along the radial direction, the exterior region is the unburnt gas region or front flame zone, and the interior is the burnt gas region or post flame zone. Fig. 8 exhibits the flow vector with heat release rate (*HRR*) distribution in the vortex-tube combustor. Given that the reaction mainly takes place upstream of the tube, points 7-12 and 60-61 are employed to analyze the specific momentum flux and its fluctuation both upstream and downstream of the reaction zone, which are also marked in Fig. 8a. Fig. 8a indicates that points 7-8 and 60 are located in the front flame zone, point 9 is on the flame front, and points 10-12 and 61 are located in the post-flame zone.

Fig. 8 indicates that when the flow field passes through the flame front, the velocity will increase. Meanwhile, the density will sharply decrease due to the *HRR* and thermal expansion. The data corresponding to the points is shown in Fig. 9. Fig. 9a displays the temperature fluctuation over time, wherein points 9-12 show a high temperature of more than 1800 K which will monotonically increase moving downstream. When moving to point 12, the corresponding temperature will reach around 2000 K, which will lead inevitably to a low density. Meanwhile, the temperature fluctuation amplitude $\triangle T$ will decrease monotonically toward the downstream, which indicates a decreased fluctuation of density.

Fig. 9b represents density fluctuation over time, which indicates that the density fluctuations correspond well to the temperature fluctuation. The density and its fluctuation amplitude will decrease monotonically downstream. From Fig. 9b, it can be seen that the density at point 8 is about 0.8 kg/m^3. Moving to point 12, the density will decrease to 0.15 kg/m^3. Additionally, the fluctuation

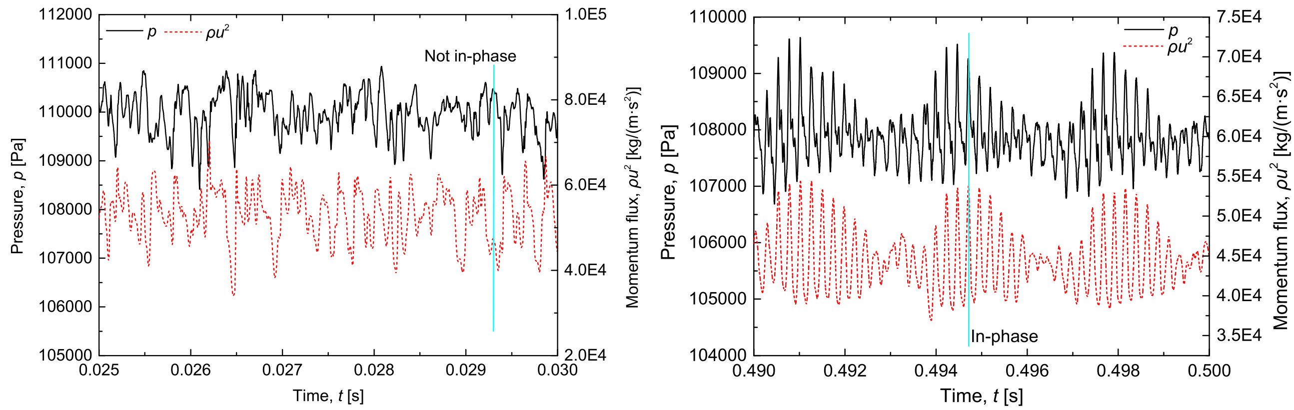

(a) Cold state

(b) Burning state

Fig. 7. The pressure and momentum flux fluctuations under cold and burning states at $q_f = 54.0$ L/min and $\varphi_g = 0.48$ in the vortex-tube combustor: (a) Cold state, (b) Burning state.

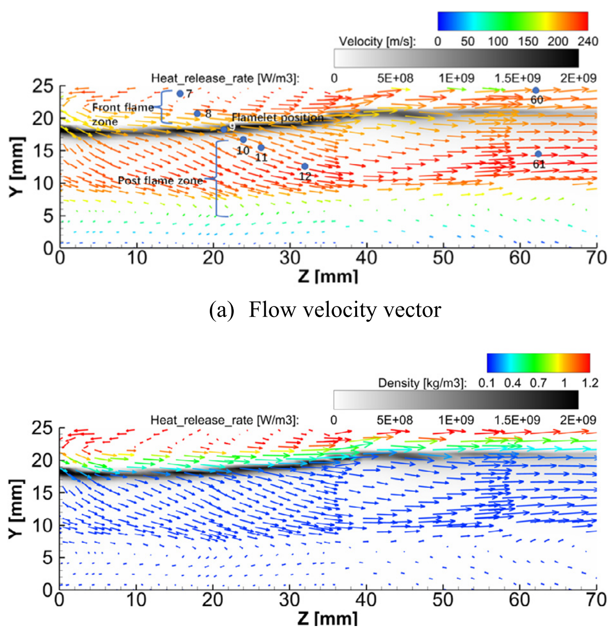

(a) Flow velocity vector

(b) Vector colored by density

Fig. 8. The flow vector with *HRR* distribution in the vortex-tube combustor and the sampling points.

amplitude is approximately 0.125 kg/m^3 at point 8, and it is only nearly 0.01 kg/m^3 at point 12. The variation of density and fluctuation amplitude will inevitably affect the momentum and its flux, and therefore affect the pressure fluctuation.

Besides the density, the flow velocity will also have an obvious influence on the momentum flux, which will affect the local static pressure as well. Based on Eq. (15), the momentum flux is proportional to the square of velocity. Thus, in theory, the effect of velocity should be greater than density. Fig. 10 shows the velocity and *HRR* fluctuations over time at different positions, which indicates that the flow velocity (u) and its fluctuation amplitude will both increase monotonically moving downstream. Fig. 10 shows that for point 8, the velocity is around 205 m/s and its fluctuation amplitude is only about 20.0 m/s. Moving to point 12, the velocity will reach up to 240.0 m/s and the fluctuation amplitude at this point can reach more than 50.0 m/s.

Moreover, the velocity phase will undergo a shift with moving downstream, indicating an opposite phase. Namely, when the flow velocity in the exterior increases, i.e., points 7-8, the flow velocity in the interior will decrease, i.e., points 9-12, indicating an opposite behavior. This should relate closely to the nature of the pressure (positive or negative) that is produced by the centrifugal force, defining it as the centrifugal force effect, which will be discussed in detail later.

Based on the analysis of the density and velocity, the momentum flux and the pressure on different points are investigated and shown in Fig. 11. Fig. 11a represents the momentum flux and its fluctuation. First, the momentum flux indicates a non-monotonical behavior. At point 7, the momentum flux is around 6.3×10^4 kg/(m · s^2), which will decrease to about 3.3×10^4 kg/(m · s^2) at point 8. Then, the momentum flux will decrease to 7.0×10^3 kg/(m · s^2) at point 9, reaching the bottommost value, and subsequently, the momentum flux will increase monotonically. When moving to point 12, the momentum flux will reach up to 8.5×10^3 kg/(m · s^2). Second, the amplitude of the momentum flux fluctuation indicates a non-monotonical behavior as well as seen in Fig. 11a. At point 7, the amplitude of the momentum flux fluctuation is around 4.0×10^4 kg/(m · s^2), which will increase to about 1.1×10^4 kg/(m · s^2) at point 8. Then, it will decrease to 3.8×10^3 kg/(m · s^2), reaching the bottommost value, and subsequently, the momentum flux will increase monotonically before point 12. When moving to point 11, the amplitude of the momentum flux fluctuation will reach up to 4.4×10^3 kg/(m · s^2). In the end, the amplitude of the momentum flux will drop to 4.0×10^3 kg/(m · s^2) again.

Fig. 11b shows pressure fluctuations over time at different positions. From this figure, it can effortlessly be observed that the pressure will decrease monotonically with moving downstream from points 7 to 12, but the corresponding fluctuation amplitude shows a non-monotonical behavior. The pressure is at its highest at point 7, yielding 108500 Pa, and the fluctuation amplitude is nearly 2000 Pa. Moving to point 8, the pressure will decrease to around 103600 Pa and the corresponding fluctuation amplitude will drop to 1050 Pa as well. Moving again to points 9-11, there is not an obvious difference between the pressure and its corresponding fluctuation amplitude at these points. At all of the points 9-11, pressure is about 102000 Pa and the corresponding fluctuation amplitude is nearly 800 Pa. When moving further to point 12, the pressure among the different points will drop to the lowest value at about 99000 Pa, however, the corresponding fluctuation amplitude shows an obvious increase, reaching up to approximately 2000 Pa.

According to Figs. 9–11, a decrease of density and an increase of flow velocity will not increase the momentum flux ρu^2, whilst the amplitude of the momentum flux downstream will not increase in the post-flame region as well. To make sense of this

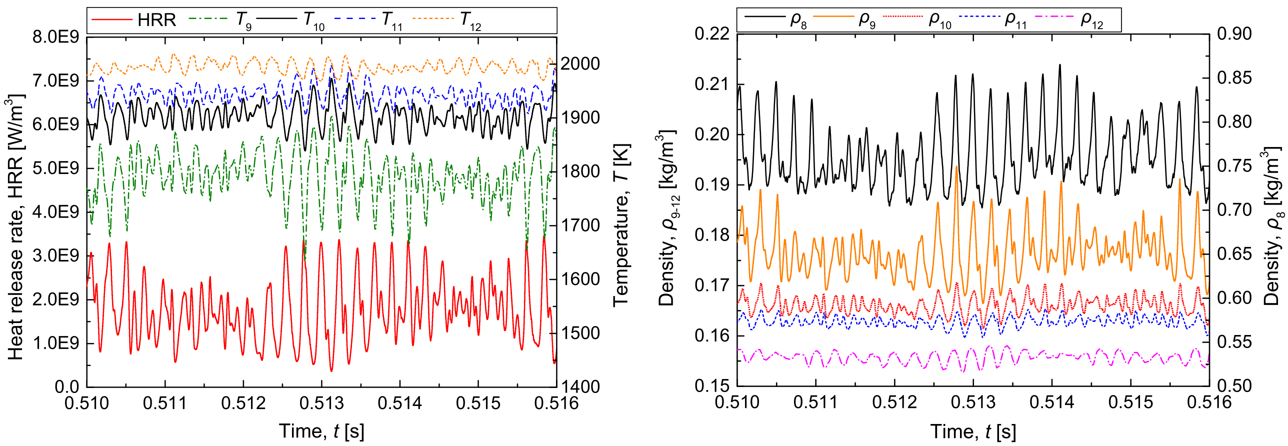

(a) Temperature with *HRR* (b) Density

Fig. 9. The temperature and density fluctuations over time at different positions.

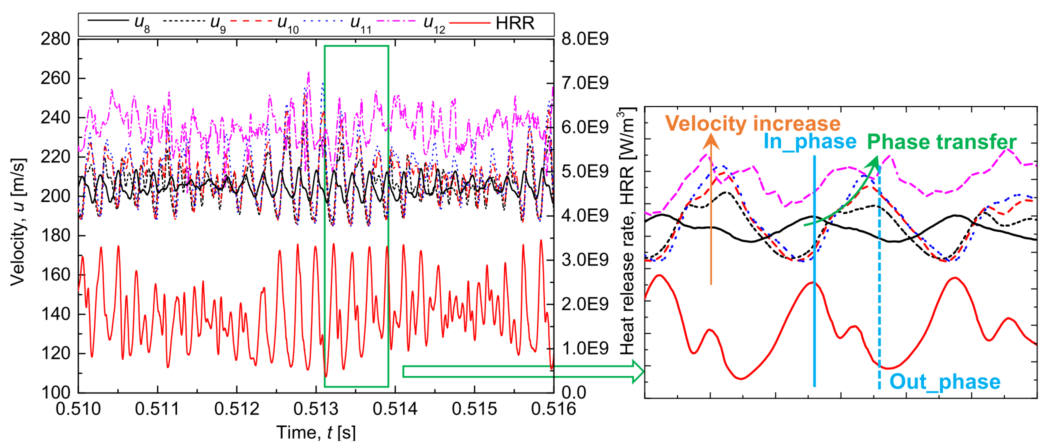

Fig. 10. The velocity and *HRR* fluctuations over time at different positions.

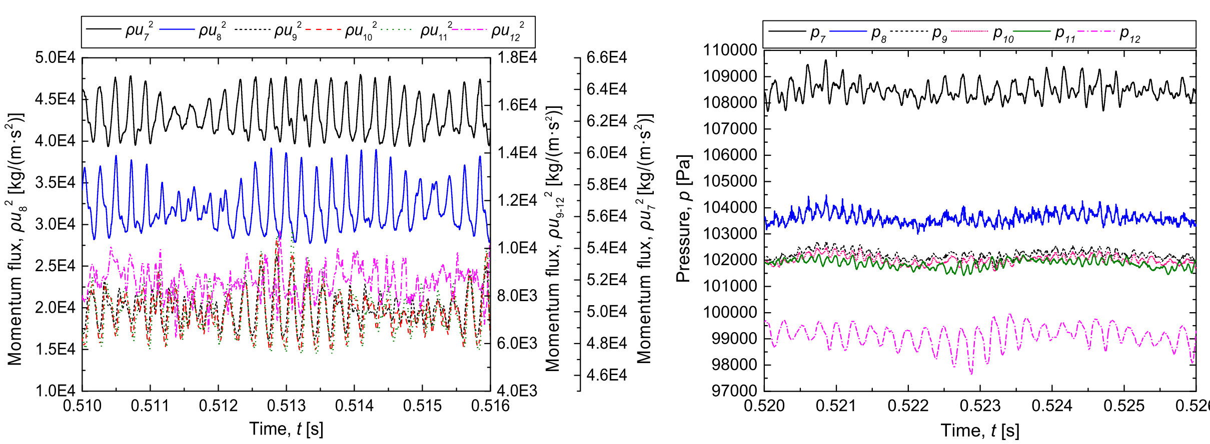

(a) Momentum flux (b) Pressure

Fig. 11. The momentum flux and pressure fluctuations over time at different positions.

phenomenon, the pressure and momentum flux distributions along the radial direction are investigated further, as shown in Fig. 12. This figure shows that the momentum and its flux will decrease rapidly along the radial direction and that this decrease occurs faster under the burning state. This is because momentum exchange is strong in the rotating environment [32,33] and its effects will become more pronounced as the viscosity of the fluid increases [34]. Given that the fluid viscosity is increased in the burning state, the momentum damping is faster. Therefore, the quick momentum damping in the vortex-tube combustor suppressed the increase of the momentum flux and its fluctuation when the *HRR* fluctuations. This is one of the principal causes of the good combustion stabilization of this vortex-tube combustor.

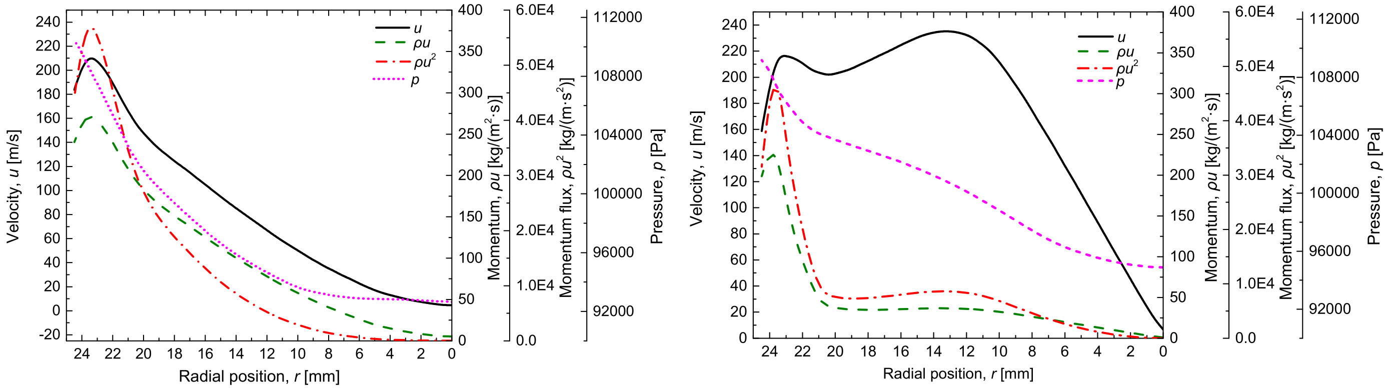

(a) Cold state　　(b) Burning state

Fig. 12. The pressure, velocity, momentum, and momentum flux distributions along the radial direction on line-60: (a) Cold state, (b) Burning state.

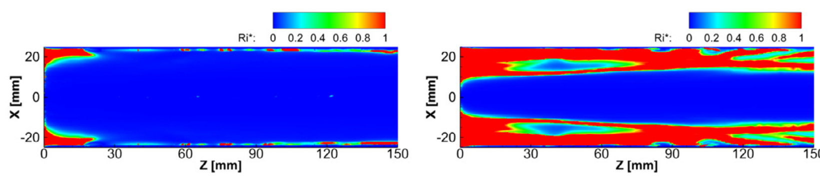

(a) Cold state　　(b) Burning state

Fig. 13. The modified Richard number R_i^* distribution at q_f = 54.0 L/min and $\varphi_g = 0.48$ in the vortex-tube combustor: (a) Cold state, (b) Burning state.

Another interesting phenomenon is that the pressure does not relate closely with the momentum flux and its fluctuation based on the momentum flux and pressure fluctuations in Fig. 11. This is because the local pressure is also affected by centrifugal force or strong rotation, which is closely related to the tangential momentum flux ρu_t^2. Given that when the momentum flux increases the pressure will generally decrease, the increase of the tangential momentum flux will also increase or reduce the pressure further. When the position locates in the exterior, where the centrifugal force will arise the pressure, i.e., points 7-8 in Fig. 8, the increase of tangential momentum flux will arise the pressure, whose function acts in reverse to that of the momentum flux in the radial and axial directions. Therefore, the momentum flux should be divided into tangential, radial, and axial components to analyze the internal relationship between momentum flux and pressure fluctuations.

4.2. Uneven attenuation and centrifugal weight

The modified Richardson number R_i^* provides an indication of the degree of aero-dynamic and thermodynamic stabilities. It provides a measure of the ratio of centrifugal forces in a field with density gradients to the inertia force and can be expressed by the following. [3]:

$$R_i^* = \frac{(1/\rho)(\partial\rho/\partial r)(u_t^2/r)}{(\partial u_a/\partial r)^2} \tag{16}$$

where ρ is the density, r is the radial position, $\partial\rho/\partial r$ is the density gradient, u_t is the tangential velocity, and u_a is the axial velocity.

When the R_i^* exceeds 1.0, the stabilization effect of centrifugal forces with density gradients is larger than the instability effect of the inertia force, which can suppress the turbulent motion and yield a laminarized fluid motion.

Fig. 13 shows that although the heat release is unsteady at q_f = 54.0 L/min and $\varphi_g = 0.48$, the R_i^* is still greater than that at the cold state due to the large density gradient, indicating laminarization of the flow field. Given that the effects of radial and axial velocities on the pressure are the same, the radial and axial velocities are merged into one, denoted by u_c, thus the corresponding momentum flux is ρu_c^2. After defining the ρu_c^2 as the radial and axial coupling (ra) momentum flux, Fig. 14 shows that the fluctuation of the ra momentum flux ρu_c^2 at the burning state is suppressed significantly due to the laminarization of the flow field, but the tangential momentum flux does not exhibit a significant decrease. Therefore, the laminarization of the flow field only suppresses the radial and axial fluctuations. Given this, the effect of the tangential momentum flux exterior exhibits an opposite behavior as compared with that of ra momentum flux ρu_c^2, whose increase will enhance the pressure. Therefore, the uneven attenuation of the momentum flux fluctuation should be the dominating cause of the larger pressure fluctuation $\triangle p$ at the burning state, rather than the enlargement of the momentum flux fluctuation $\triangle\rho u^2$. To put it concretely, the fluctuation amplitude of the tangential momentum flux ρu_t^2 at the cold state is approximately 2.0×10^4 kg/(m · s^2), which is larger than that at the burning state of around 1.6×10^4 kg/(m · s^2), indicating a larger pressure fluctuation resulting from the larger fluctuation of centrifugal force. The fluctuation of the ra momentum flux $\triangle\rho u_c^2$ at the cold state is about 3×10^3 kg/(m · s^2). Based on this, the fluctuations of the tangential and ra momentum fluxes are in phase, therefore the large $\triangle\rho u_c^2$ will decrease the pressure. However, the $\triangle\rho u_c^2$ at the burning state is just 5×10^2 kg/(m · s^2), so its inhibition of the pressure increase resulting from the increase of ρu_t^2 is limited, yielding a relatively large pressure fluctuation $\triangle p$.

Given the uneven attenuation of the momentum flux fluctuation at point 60, as discussed above, the $\triangle\rho u_c^2$ and $\triangle\rho u_t^2$ at points 7-12 and 61 are investigated further to better understand the coupling influence of the fluctuations of the tangential and ra momentum fluxes on the pressure fluctuation as seen in Fig. 14. The purpose of this investigation is to explain why the pressure does not relate closely with the total momentum flux $\triangle\rho u^2$, as shown in Fig. 11.

In Fig. 15, for point 7, it can be seen that the fluctuation of the tangential momentum flux $\triangle\rho u_t^2$ is around 4×10^3 kg/(m · s^2), which is obviously smaller than that at point 60. Meanwhile, the

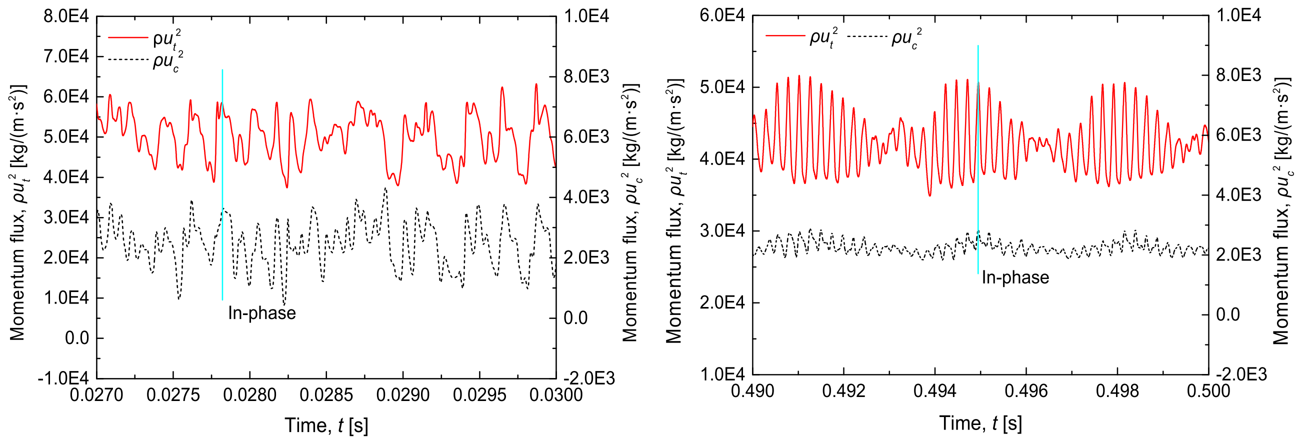

(a) Cold state (b) Burning state

Fig. 14. The fluctuations of the tangential and axial momentum flux at point 60: (a) Cold state, (b) Burning state.

fluctuation of *ra* momentum flux $\triangle\rho u_c^2$ is also very small. Thus, the decreased $\triangle\rho u_t^2$ results in a decreased pressure fluctuation $\triangle p$ of around 1700 Pa. Moving downstream to point 8, another interesting phenomenon occurs. It can be seen that the $\triangle\rho u_t^2$ will reach up to around 1.0×10^4 kg/(m $\cdot$ s^2) at point 8, however, the pressure fluctuation amplitude $\triangle p$ is just 1050 Pa. Although the $\triangle\rho u_c^2$ will increase to 4×10^2 kg/(m $\cdot$ s^2), its effect is slight. Thus, the centrifugal effect is weak at this point. With moving to points 9 and 11, the $\triangle\rho u_c^2$ does not represent an obvious difference, as are all around 3×10^2 kg/(m $\cdot$ s^2), but the fluctuation of the tangential momentum flux $\triangle\rho u_t^2$ will decrease to around 3×10^3 kg/(m $\cdot$ s^2) and the $\triangle p$ decreases to its bottommost value of nearly 800 Pa. Besides the small $\triangle\rho u_t^2$, the position should also be responsible for the low-pressure fluctuations at these points. Point 10 is neglected in this section because its fluctuation properties are similar to that of points 9 and 11. Moving further downstream to point 12, the pressure fluctuation $\triangle p$ will reach up to about 2000 Pa again. Given that the $\triangle\rho u_t^2$ and $\triangle\rho u_c^2$ do not represent an obvious difference when compared with points 9 and 11, the effect of the $\triangle\rho u_t^2$ has changed, defining it as the centrifugal effect, becoming obvious again at point 12. The fluctuation information at point 61 further supports our findings. Therefore, the centrifugal effect relates closely to the radial position, which has an important influence on the pressure fluctuation $\triangle p$. Namely, the effect of the same fluctuation amplitude of tangential momentum flux $\triangle\rho u_t^2$ is different in different positions.

Consequently, given the above findings, we put forward a new parameter called the centrifugal weight coefficient, denoted as λ, which can be calculated according to Eq. (17). When $\lambda > 0$, the centrifugal effect, based on the $\triangle\rho u_t^2$ and radial position, will overcome the pressure drop due to the increase of $\triangle\rho u_t^2$, defining it as the velocity effect and then yielding an increased pressure. When $\lambda < 0$, the centrifugal effect will also decrease the pressure with the velocity effect, yielding a decreased pressure. When $\lambda = 0$, an increase in pressure caused by the centrifugal effect is equal to the pressure drop caused by the velocity or momentum flux increases.

$$\lambda = \frac{p - p_0}{p_k - p_0} \tag{17}$$

where p is the local pressure in a flow field, p_0 is the local pressure that ignores the effect of centrifugal force, and p_k is the peak pressure.

This Eq. (17) is suitable for both the cold and burning states. Figs. 10 and 11 indicate that the pressure fluctuation on different points is in phase, while the velocity is out-phase. Given this, in the $\lambda > 0$ region, an increase of the tangential momentum flux $\triangle\rho u_t^2$ will increase the pressure; in the $\lambda < 0$ region, an increase of the $\triangle\rho u_t^2$ will decrease the pressure. Given that the $\triangle\rho u_t^2$ only decreases in the interior $\lambda < 0$ region, the pressure will increase and the $\lambda = 0$ position is also where the phase transfer occurs, which is in good agreement with that which was derived based on Eq. (17).

According to Eq. (17), Fig. 16 shows the contour of centrifugal weight coefficient λ distribution in the vortex-tube combustor in the case of $q_f = 54.0$ L/min and $\varphi_g = 0.48$. It is notable that the λ decreases monotonically along the radial direction from the tube wall to the center. In the 20 $\sim$ 25 mm and 10 $\sim$ 14 mm region, the $|\lambda|$ is large and approaches 1.0. An increase of $|\lambda|$ indicates that the centrifugal effect on the pressure will increase and vice versa. So, the cause of different centrifugal effects is the variation of the centrifugal weight coefficient $|\lambda|$. The λ at points 7, 12, and 60 are 0.86, -0.44, and 0.77 respectively, which are all far away from zero. This is the principal reason for the large $\triangle p$ at points 7, 12, and 60. In like manner, the λ at points 8, 9, 10, 11, and 61 are 0.11, -0.04, -0.05, -0.09, and -0.2, respectively, none of which are far from zero. This is the principal reason for the weak pressure fluctuation at points 8-11 and 61.

5. Summary and conclusions

In this work, the pressure, density, and momentum flux at different points in a vortex-tube combustor were investigated to analyze the response mechanism of the pressure fluctuation to the unsteady heat release rate (*HRR*) in a strong rotating environment via a LES simulation method. Results show that the resultant amplitude of the pressure fluctuation $\triangle p$ mainly depends on the momentum fluxes in the different directions, as well as the centrifugal weight coefficient. The specific conclusions are summarized as follows:

1. The peak amplitudes of pressure and *HRR* fluctuations at the 'unsteady' state can reach 3000 Pa and 2.8×10^6 W/m^3, whilst the Rayleigh parameter $Ra(x)$ is 6.98×10^{-2}. These are significantly greater than that at the steady state. The pressure fluctuation in the burning state is also larger than that in the cold state, even though the degree of fluid laminarization for the former is higher, the degree of pressure fluctuation is still not intense.
2. The pressure is not closely related to the momentum flux and its fluctuation; this is due to the effect of the centrifugal force

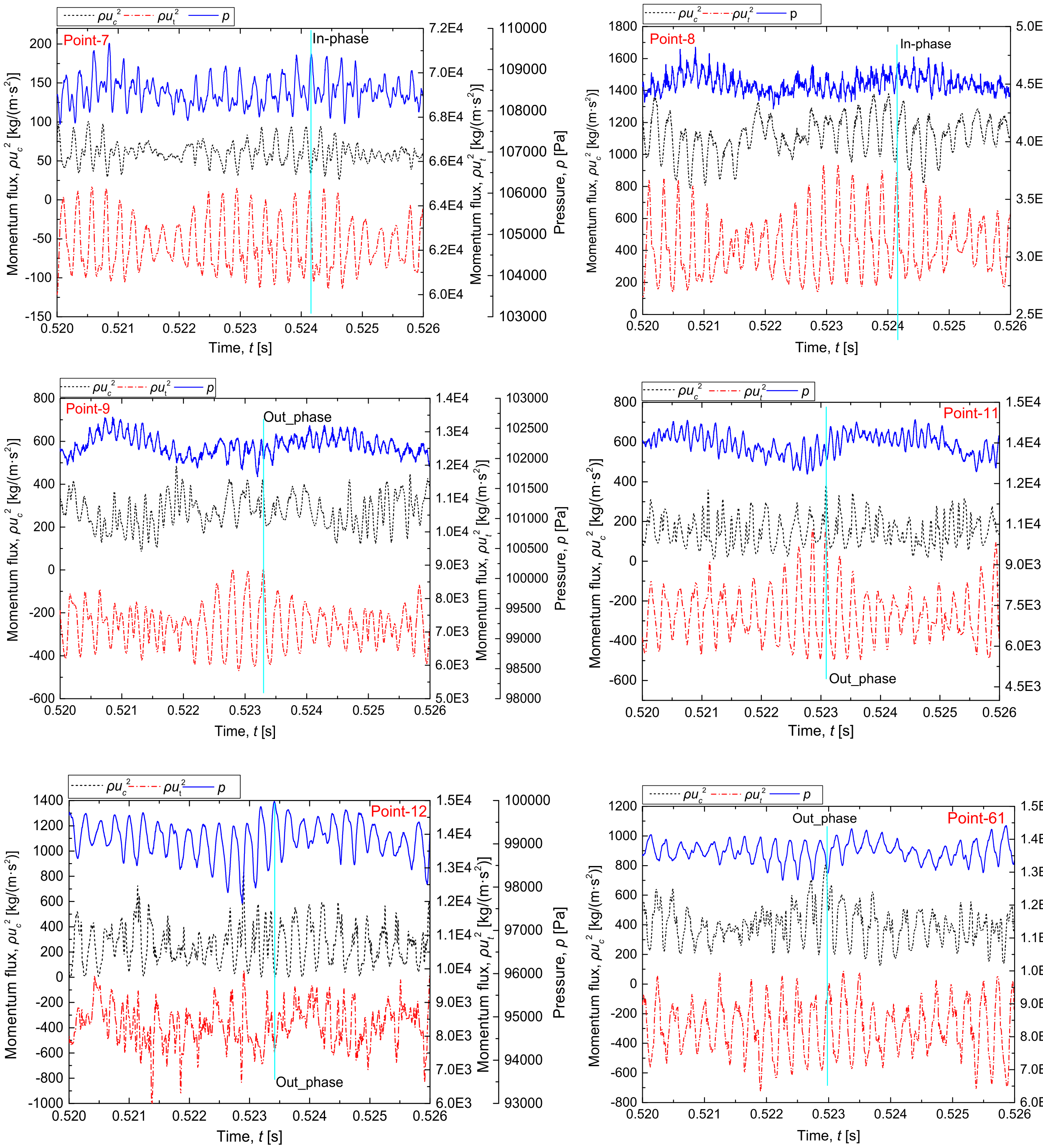

Fig. 15. The fluctuations of the momentum flux and pressure on different positions.

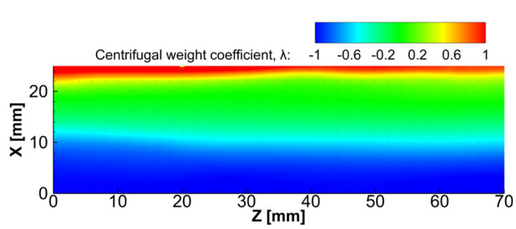

Fig. 16. The centrifugal weight coefficient distribution where $q_f = 54.0$ L/min and $\varphi_g = 0.48$.

or the rotating behavior. By splitting the momentum flux into its tangential and *ra* (radial plus axial) components, we find that the tangential momentum flux ρu_t^2 acts in a manner opposite to that of the radial and axial directions in the exterior region, viz, the increase of tangential momentum flux will increase the pressure, while the pressure will decrease for the radial and axial situations.

3. The momentum flux and its fluctuation do not indicate a higher value at the 'unsteady' burning state due to quick momentum damping along the radial direction. The laminarization of the flow field only suppresses fluctuations in the radial and axial directions. The resultant uneven attenuation of the momentum flux fluctuation is the dominant cause of the larger pressure fluctuation $\triangle p$ at the 'unsteady' burning state because the effect of the *ra* momentum flux is suppressed.

4. The cause of different centrifugal effects is the variation of the centrifugal weight coefficient λ. When the λ value is far from zero, the centrifugal effect will be obvious, resulting in a large pressure fluctuation $\triangle p$, whereas when the λ value approaches zero, the centrifugal effect is weak, yielding a small pressure fluctuation $\triangle p$.

Therefore, if we want to suppress the pressure fluctuation and obtain an ultra-steady combustion process, an extra disturbance is required in the exterior region in a strong rotating environment, which is not difficult to implement in practice.

Declaration of competing interest

The authors declare that they have no known competing financial interests or personal relationships that could have appeared to influence the work reported in this paper.

Data availability

No data was used for the research described in the article.

Acknowledgement

This research has been funded by the postdoctoral program of the International Training Program for Outstanding Young Scientific Research Talents of Guangdong Province of China and the Engineering and Physical Sciences Research Council (EPSRC) through the UK Consortium on Turbulent Reacting Flow (UKCTRF) [Grant number: EP/K025163/1] used the ARCHER UK National Supercomputing Service (http://www.archer.ac.uk). Computing resources were also provided by the HPC, Imperial College London.

References

[1] K.M. Lyons, Toward an understanding of the stabilization mechanisms of lifted turbulent jet flames: experiments, Prog. Energy Combust. Sci. 33 (2007) 211–231.
[2] S.J. Ren, H.L. Yang, L.Q. Jiang, D.Q. Zhao, X.H. Wang, Combustion modes and driving mechanisms of pressure fluctuation in a novel vortex-tube combustor with quasi-steady and stratified properties, Exp. Therm. Fluid Sci. 117 (2020) 110134.
[3] J.M. Beér, N.A. Chigier, T.W. Davies, K. Bassindale, Laminarization of turbulent flames in rotating environments, Combust. Flame 16 (1971) 39–45.
[4] N. Syred, J.M. Beer, Combustion in swirling flows: a review, Combust. Flame 23 (1974) 143–201.
[5] T.C. Lieuwen, Unsteady Combustor Physics, Cambridge University Press, 2012.
[6] T.C. Lieuwen, V. Yang, Combustion instabilities in gas turbine engines: operational experience, fundamental mechanisms, and modeling, Mech. Eng. 128 (2015).
[7] T. Schuller, D. Durox, S. Candel, A unified model for the prediction of laminar flame transfer functions: comparisons between conical and V-flame dynamics, Combust. Flame 134 (2003) 21–34.
[8] A. Scholtissek, R.W. Pitz, C. Hasse, Flamelet budget and regime analysis for non-premixed tubular flames, Proc. Combust. Inst. 36 (2017) 1349–1356.
[9] X.S. Han, A.S. Morgans, Simulation of the flame describing function of a turbulent premixed flame using an open-source LES solver, Combust. Flame 162 (2015) 1778–1792.
[10] T.C. Lieuwen, H. Torres, C. Johnson, B.T. Zinn, A mechanism of combustion instability in lean premixed gas turbine combustors, J. Eng. Gas Turbines Power 123 (1999) 182.
[11] N. Magina, D.-H. Shin, V. Acharya, T. Lieuwen, Response of non-premixed flames to bulk flow perturbations, Proc. Combust. Inst. 34 (2013) 963–971.
[12] L. Davidson, Fluid mechanics, turbulent flow and turbulence modeling, 2015.
[13] S. Ishizuka, On the behavior of premixed flames in a rotation flow field establishment of tubular flames, Symp., Int., Combust. 1 (1985) 287–294.
[14] S.J. Ren, H.L. Yang, L.Q. Jiang, D.Q. Zhao, X.H. Wang, Stabilization characteristics and mechanisms in a novel tubular flame burner with localized stratified property, Energy 197 (2020) 117235.
[15] T.C. Lieuwen, V. Yang, Combustion instabilities in gas turbine engines: operational experience, fundamental mechanisms, and modeling, AIAA J. (2005).
[16] T.F. Lu, C.K. Law, A criterion based on computational singular perturbation for the identification of quasi steady state species: a reduced mechanism for methane oxidation with NO chemistry, Combust. Flame 154 (2008) 761–774.
[17] A. Bhagatwala, J.H. Chen, T.F. Lu, Direct numerical simulations of HCCI/SACI with ethanol, Combust. Flame 161 (2014) 1826–1841.
[18] R.S. Barlow, A.N. Karpetis, J.H. Frank, J.Y. Chen, Scalar profiles and NO formation in laminar opposed-flow partially premixed methane/air flames, Combust. Flame 127 (2001) 2102–2118.
[19] J. Smagorinsky, General circulation experiments with the primitive equations: I. The basic experiment, Mon. Weather Rev. 91 (1963) 99–164.
[20] W.P. Jones, S. Navarro-Martinez, Study of hydrogen auto-ignition in a turbulent air co-flow using a Large Eddy Simulation approach, Comput. Fluids 37 (2008) 802–808.
[21] T. Brauner, W.P. Jones, A.J. Marquis, LES of the Cambridge stratified swirl burner using a sub-grid pdf approach, Flow Turbul. Combust. 96 (2016) 965–985.
[22] F. Gao, E.E. O'Brien, A large-eddy simulation scheme for turbulent reacting flows, Phys. Fluids A, Fluid Dyn. 5 (1993) 1282–1284.
[23] F.A. Jaberi, P.J. Colucci, S. James, P. Givi, S.B. Pope, Filtered mass density function for large-eddy simulation of turbulent reacting flows, J. Fluid Mech. 401 (1999) 85–121.
[24] W.P. Jones, S. Navarro-Martinez, Large eddy simulation of autoignition with a subgrid probability density function method, Combust. Flame 150 (2007) 170–187.
[25] N. Branley, W.P. Jones, Large eddy simulation of a turbulent non-premixed flame, Combust. Flame 127 (2001) 1914–1934.
[26] U. Piomelli, J.H. Liu, Large-eddy simulation of rotating channel flows using a localized dynamic model, Phys. Fluids 7 (1995) 839–848.
[27] W.P. Jones, V.N. Prasad, Large Eddy Simulation of the Sandia Flame Series (D–F) using the Eulerian stochastic field method, Combust. Flame 157 (2010) 1621–1636.
[28] L. Valino, A field Monte Carlo formulation for calculating the probability density function of a single scalar in a turbulent flow, Flow Turbul. Combust. 60 (1998) 157–172.
[29] S.J. Ren, W.P. Jones, X.H. Wang, Stabilization mechanism revelation of an novel vortex-tube combustion technique: LES with sgs-pdf approach, Phys. Fluids (2022), https://doi.org/10.1063/5.0090978.
[30] S.J. Ren, L.Q. Jiang, H.L. Yang, D.Q. Zhao, X.H. Wang, Comparative study on the combustion performance in localized stratified and rapidly mixed swirling tubular flame burners, Combust. Sci. Technol. 8 (2019) 1444–1462.
[31] V. McDonell, 5 - Lean combustion in gas turbines, in: D. Dunn-Rankin, P. Therkelsen (Eds.), Lean Combustion, second edition, Academic Press, Boston, 2016, pp. 147–201.
[32] N. Syred, A review of oscillation mechanisms and the role of the precessing vortex core (PVC) in swirl combustion systems, Prog. Energy Combust. Sci. 32 (2006) 93–161.
[33] S. Ishizuka, Characteristics of tubular flames, Prog. Energy Combust. Sci. 19 (1993) 187–226.
[34] C.K. Law, Combustion Physics, Cambridge University Press, Cambridge, 2006.